Journal of Electrostatics 112 (2021) 103591

Contents lists available at ScienceDirect

Journal of Electrostatics

journal homepage: www.elsevier.com/locate/elstat

Estimating droplet charge in numerical simulations of charged sprays

Antoni Brentjes *, Artur K. Pozarlik, Gerrit Brem

Department of Thermal and Fluid Engineering, University of Twente, Enschede, The Netherlands

ARTICLE INFO

Keywords:
Electrostatic spray
Computational fluid dynamics
Droplet charge
Spray current

ABSTRACT

A novel method for estimating droplet charge in numerical simulations of conductively and inductively charged sprays is presented. This method is based on balancing the effective electric field at the sprayer nozzle with the global electric field induced by the charged droplets. The global approach avoids the need for computationally expensive local resolution of the spray formation region, allowing it to be used in Eulerian–Lagrangian simulations of high-flowrate sprays. The method is validated against experimental data from literature, proving it can predict droplet charge with reasonable engineering accuracy, over a wide range of spray parameters, for conductive spray liquids.

1. Introduction

Electrically charged sprays presently exist in a plethora of sizes, forms, and applications [1]. Compared to uncharged sprays, they offer several industrially advantageous properties, with the most prominent being the improved transfer efficiency and self-dispersal of the spray. As such they are commonly used in painting and coating systems, gas scrubbers, cooling systems, and fuel atomisers, in addition to various more niche and specialised applications. Substantial amounts of experimental and applied research has been carried out on charged sprays, and a large library of theoretical and numerical models exists, describing these sprays' behaviour. However, full physics modelling of high-flowrate sprays is not yet possible, leaving some significant gaps in our knowledge. Indeed a common complaint in numerical research articles is the lack of a good method for predicting the droplet charge in directly charged sprays [2,3]. The droplet charges are usually estimated based on experimental data (authors' own measurements [4] or from literature [2]), or not even discussed [5]. While measurements are an excellent way of obtaining this data, a major motivation for doing numerical simulations is to avoid the need for experiments in the first place.

In this paper, we propose an efficient numerical approach for estimating droplet charge in directly-charged, high-flowrate sprays. In this context, direct charging means the spray liquid takes on charge via conductive contact with an electrode. This is in contrast to external charging methods such as corona charging, for which some numerical models already exist [1,6]. Our distinction between high- and low-flowrate sprays is based on computational limitations. For capillary electrosprays with flowrates on the order of millilitres per hour, Collins et al. [7], Herrada et al. [8], and Wei et al. [9] have shown the feasibility of simulating the jet breakup and droplet formation using Volume of Fluid based methods. Such a detailed simulation would be impractical if not impossible when modelling industrial processes such as spray painting, with flowrates often exceeding 100 millilitres per minute. The common approach to such problems is to use Lagrangian particle tracking instead, which is therefore also used in our model.

Since simulating the full physics is not possible, our model needs to work on more general principles. Jaworek [1] gives a comprehensive overview of the theory of direct charging of sprays. The core mechanism is that electrostatic interactions push charges to the surface of the liquid jet at a spray nozzle. As the jet breaks up, the resultant ligaments and droplets carry these charges with them. For sufficiently conductive liquids, the charge density on the jet surface is directly proportional to the local electric field strength. Thus, the key to determining the droplet charge for a given sprayer lies in finding the electric field strength around the spray breakup zone.

Computation of the electric field in a simulation of charged sprays is rather straightforward and indeed included in most works on this topic. The simulation framework we use is described in detail in our previous work [10], but our method for charge estimation is not exclusive to that framework. Instead we will show a general approach to determine droplet charges based on electric field solutions, and discuss stable implementation of this approach in iterative solvers. Finally, to demonstrate the accuracy and versatility of our method, we perform two simulations validated against measurement data from literature.

2. Modelling approach

The charge density on the surface of a conductive liquid is directly proportional to the local electric field intensity. This follows directly

* Corresponding author.
E-mail addresses: a.brentjes@utwente.nl (A. Brentjes), a.k.pozarlik@utwente.nl (A.K. Pozarlik), g.brem@utwente.nl (G. Brem).

https://doi.org/10.1016/j.elstat.2021.103591
Received 27 January 2021; Received in revised form 24 March 2021; Accepted 9 April 2021
Available online 19 April 2021

Table 1
Boundary conditions for the potential field components.

Component	Nozzle	Conductors	Symmetry planes
Ψ_e	$\Psi_e = \Psi - \Psi_d - \Psi_0$	$\Psi_e = 0$	$\frac{\partial}{\partial n}\Psi_e = 0$
Ψ_d	$\frac{\partial}{\partial n}\Psi_d = 0$	$\Psi_d = 0$	$\frac{\partial}{\partial n}\Psi_d = 0$
Ψ_0	$\frac{\partial}{\partial n}\Psi_0 = 0$	$\Psi_0 = \Psi$	$\frac{\partial}{\partial n}\Psi_0 = 0$

from the Poisson equation (1) governing the electrostatic field and Gauss' Law. Using this principle to directly calculate droplet charge requires full resolution of the liquid jet breakup, which is unfortunately not feasible for high-flowrate sprays. It does, however, give us a more pragmatic insight. If each individual droplet's charge depends linearly on the electric field intensity, then so must the charge of the bulk of the spray. This, indeed, forms the central principle of our model.

The second key component of our model is the space-charge effect created by the cloud of charged spray droplets. This space charge effect has a significant influence on the electric field in the sprayer–target system, as shown by Ellwood and Braslaw [2]. Furthermore, Wei et al. [9] show that this effect can significantly reduce the intensity of the electric field near the sprayer, reducing the charge on subsequently emitted droplets. This can be seen as a self-limiting mechanism for spray charge.

2.1. Model definitions

The electrostatic field is governed by the Poisson equation (1) given below.

$$\vec{\nabla}^2\Psi = \frac{\rho_q}{\epsilon_0} \quad \text{with} \quad \vec{E} = -\vec{\nabla}\Psi \tag{1}$$

Here Ψ denotes the electric potential, $\vec{E}$ the electric field, ρ_q the charge density, and ϵ_0 the permittivity of the vacuum. Since this equation is linear, the potential field can be split into separate components by the principle of superposition. We want to isolate the field intensity at the spray nozzle, and the effect of space charge, and therefore choose the following components:

$$\begin{aligned} \Psi &= \Psi_0 + \Psi_d + \Psi_e \\ \vec{\nabla}^2\Psi_0 = \vec{\nabla}^2\Psi_e &= \vec{\nabla}^2\Psi_d - \frac{\rho_q}{\epsilon_0} = 0 \end{aligned} \tag{2}$$

Here Ψ_d is the potential field generated by the charged droplets, Ψ_e is the effective potential field generated by the spray nozzle, and Ψ_0 represents the effects of all other electrified bodies. To prevent Ψ_d and Ψ_0 from contributing to the field intensity at the nozzle, a zero flux boundary condition is applied at the nozzle for those field components. This may result in non-zero potentials, which are compensated for in the boundary conditions for Ψ_e. Finally, since Ψ_0 represents all electrified bodies, all other boundary conditions for Ψ_e and Ψ_d are set to 0. These conditions are summarised in Table 1.

Working on the principle that the charge of the bulk of the spray is proportional to the field intensity at the nozzle, and having isolated this intensity to the Ψ_e field component, we can start building our model equations. First, for convenience, we define the Effective Nozzle Potential $\psi_e = \Psi_e|_{nozzle}$. Next, since droplet charges depend on the particle diameter in polydisperse sprays, we express the bulk spray charge in the form of a spray current I_s. Both of these are treated as quasi-steady variables, with a linear relation as given in Eq. (3).

$$I_s = \psi_e * f(\ldots) \quad \text{with} \quad \psi_e = \Psi_e|_{nozzle} \tag{3}$$

The constant of proportionality in this equation is $f(\ldots)$, a yet-to-be-determined function of the sprayer and spray parameters, that is independent of ψ_e.

For a given set of droplet trajectories, the space charge density throughout the domain, and therefore the magnitude of Ψ_d, is linear with the spray current I_s. This we can express as Eq. (4).

$$\psi_d = I_s * g(\ldots) \quad \text{with} \quad \psi_d = \Psi_d|_{nozzle} \tag{4}$$

Here $g(\ldots)$ is a function based on the field solution of the Ψ_d potential component, and is notionally independent of I_s. It must be noted that the spray droplet trajectories are not truly independent of the droplet charge, but in the steady or quasi-steady case Eq. (4) must nevertheless hold.

From Eq. (2) and our boundary conditions it follows that the potential at the spray nozzle must satisfy:

$$\psi = \psi_0 + \psi_d + \psi_e \quad \text{with} \quad \psi_0 = \Psi_0|_{nozzle} \tag{5}$$

Combining Eqs. (3)–(5) we can thus formulate a general expression for the spray current I_s:

$$I_s = (\psi - \psi_0)\frac{f(\ldots)}{1 + f(\ldots)g(\ldots)} \tag{6}$$

To make this equation into a useful model we must now find suitable ways of determining the values of f and g, our functions of proportionality.

2.2. Spray current as a function of effective nozzle potential

The amount of current imparted to the spray is proportional with the effective potential (or electric field intensity) at the nozzle. The coefficient of proportionality is determined by the geometry of the sprayer nozzle and the flow rate and breakup pattern of the liquid jet. The accuracy to which its value can be approximated depends on how well the geometry and flow of the jet are understood. Some approximations exist, such as the one given by Jaworek [1] for induction-charging pressure atomisers. We find that, for sprayers using a central orifice nozzle, sufficiently accurate results can be obtained by approximating the geometry of the sprayer and fluid as two touching spheres. The electric charge distribution for this approximate geometry can be solved analytically, as presented in the following sections. For sprayers that produce droplets along a linear or toroidal "nozzle", such as rotating bell sprayers, an analogous two-cylinder or concentric-torus solution may be derived in similar fashion.

2.2.1. Solution of infinite images

The charge of the spray droplets is determined at the moment of primary breakup, after which no more current can be conducted into the droplet. We approximate the liquid's geometry at primary breakup with two spherical bodies, one of which represents the bulk, and the other representing the detaching mass. The electric potential of both spheres is equal, based on the assumption that the liquid is sufficiently conductive. This may be checked by comparing the electric relaxation time to the hydrodynamic time scale, a criterion given by Marchewicz et al. [11] and shown in Eq. (7). Here, ϵ denotes the permittivity of the liquid, σ the conductivity of the liquid, d_{nozzle} the sprayer nozzle diameter and Q the volumetric flowrate of the spray.

$$\tau_{el} \ll \tau_h \quad \text{with} \quad \tau_{el} = \frac{\epsilon}{\sigma} \quad \text{and} \quad \tau_h = \frac{d_{nozzle}}{u} = \frac{\pi d_{nozzle}^3}{4Q} \tag{7}$$

We know that the electric field around a sphere at a constant potential ψ_s is identical to the field generated by a point charge of magnitude $q_s = \psi_s R_s/k$ with $k = (4\pi\epsilon_0)^{-1}$, located at the centre of the sphere. The method of image charges [12] dictates that a point-charge located near a conductive sphere induces an image charge inside the sphere. Thus, two conductive spheres kept at constant potential in close proximity will mutually induce image charges. These image charges recursively induce further image charges, and the total charge on either sphere may be found by taking the sum of these, through the so-called method of infinite images.

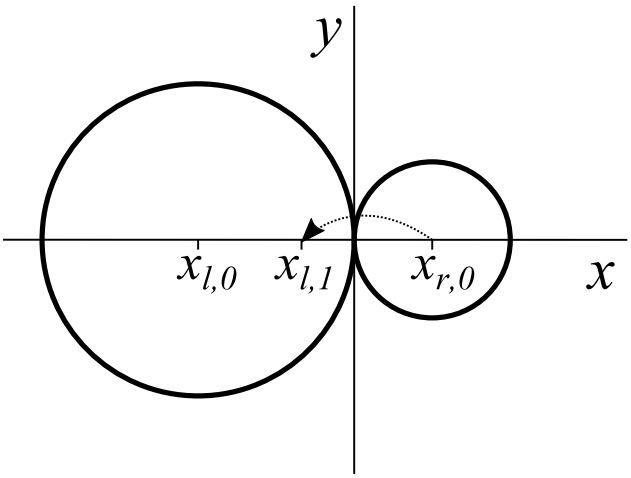

Fig. 1. Two sphere geometry and first induced image charge location.

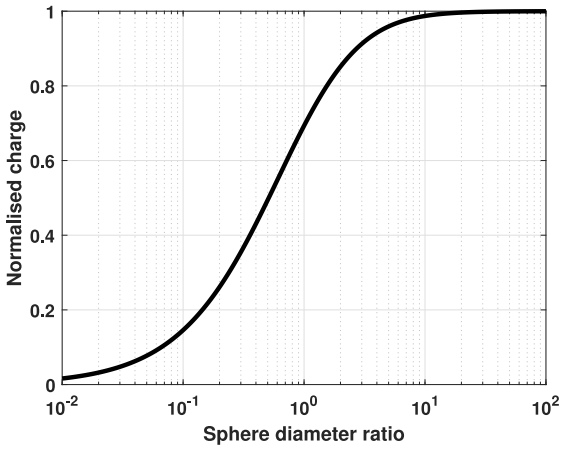

Fig. 2. Normalised charge on right sphere, $Q_r k/\psi_e R_r$, as a function of diameter ratio a.

The geometry and system of coordinates are defined as shown in Fig. 1. Two spheres are placed with their centres on the x-axis, such that they make tangential contact in the origin. The x-coordinates of the initial point-charges, at the centres of the spheres, are thus $x_{l,0} = -R_l$ and $x_{r,0} = R_r$. These initial charges we name $q_{l,0}$ and $q_{r,0}$, for the left and right spheres respectively. As a matter of definition, charge $q_{l,n+1}$ is located in the left sphere, and is the image of charge $q_{r,n}$, and vice versa. The locations of these charges are correspondingly called $x_{l,n+1}$ and $x_{r,n}$. Eq. (8) gives a recursive relation for the positions of the image charges in our coordinate system.

$$x_{l,n+1} = -\frac{x_{r,n}\,R_l}{x_{r,n} + R_l} \quad \text{and} \quad x_{r,n+1} = \frac{x_{l,n}\,R_r}{x_{l,n} - R_r} \tag{8}$$

For simplicity we define the ratio between the radii of the spheres a such that $R_r = aR_l$. It can then be trivially shown that Eq. (8) and the defined geometry are satisfied by the solutions:

$$x_{l,n} = \begin{cases} \dfrac{-R_l}{1 + m(1 + a^{-1})} & \text{if } n = 2m \\ \dfrac{-R_l}{(m+1)(1 + a^{-1})} & \text{if } n = 2m + 1 \end{cases} \quad \text{and}$$

$$x_{r,n} = \begin{cases} \dfrac{R_r}{1 + m(1 + a)} & \text{if } n = 2m \\ \dfrac{R_r}{(m+1)(1 + a)} & \text{if } n = 2m + 1 \end{cases} \tag{9}$$

The magnitude of the image charges can be recursively expressed as (10).

$$q_{l,n+1} = \frac{-q_{r,n}R_l}{x_{r,n} + R_l} \quad \text{and} \quad q_{r,n+1} = \frac{q_{l,n}R_r}{x_{l,n} - R_r} \tag{10}$$

The initial charge on either sphere is chosen so that it produces an electric potential ψ_e at the surface of the sphere, thus $q_{l,0} = \psi_e R_l/k$ and $q_{r,0} = \psi_e R_r/k$. Noting that Eq. (10) is similar in structure to Eq. (8), and the initial charges and initial positions both scale with the radius of the sphere in question, the strength of the image charges will be proportional with their positions. Indeed it can be shown that the solution expressed in Eq. (11) satisfies Eq. (10) and the given initial values.

$$q_{l,n} = -1^n \frac{\psi_e}{k}|x_{l,n}| \quad \text{and} \quad q_{r,n} = -1^n \frac{\psi_e}{k}|x_{r,n}| \tag{11}$$

2.2.2. Sum of infinite images

The total charge of either sphere can be computed by taking the sum of the initial charge and all image charges induced on the sphere. That is, $Q_l = \sum_{n=0}^{\infty} q_{l,n}$ and similarly with r subscripts for the right sphere. Assuming both spheres' radii are finite, the sum of the series of Eq. (11) converges. In the special case of $a = 1$, i.e. both spheres having equal radii, this series effectively becomes an alternating harmonic series, and we find $Q_l = Q_r = \ln(2)\psi_e R/k$.

If the spheres do not have equal radii, the sum can be rewritten into the formulation of Eq. (12). Only the expression for Q_r is given, to obtain Q_l, R_r and a should be replaced with R_l and a^{-1} respectively.

$$Q_r = \frac{\psi_e R_r}{k}\left[\frac{1}{1+a}\sum_{m=0}^{\infty}\left(\frac{1}{m + (1+a)^{-1}} - \frac{1}{m+1}\right)\right] \tag{12}$$

Abrahamowitz [13] gives an exact solution for sums of this nature, and we can find the following results for charges Q_l and Q_r:

$$Q_l = \frac{-\psi_e R_l}{k(1 + a^{-1})}\left[\gamma + F\left(\frac{1}{1 + a^{-1}}\right)\right] \quad \text{and}$$

$$Q_r = \frac{-\psi_e R_r}{k(1 + a)}\left[\gamma + F\left(\frac{1}{1 + a}\right)\right] \tag{13}$$

Here γ denotes the Euler–Mascheroni constant, and F the Digamma function (or logarithmic derivative of the Gamma function). To illustrate, Fig. 2 shows the normalised charge of the right sphere, $Q_r k/\psi_e R_r$. As seen in the figure, for equally sized spheres, their normalised charge is equal to ln(2). For unequal spheres, the normalised charge asymptotically approaches zero for the smaller sphere and one for the larger sphere, as the diameter ratio increases.

2.2.3. Computing spray current

In this model we assume that the left of the two spheres represents the nozzle and liquid bulk, and the right sphere represents masses of liquid detaching during primary breakup. The charge of each detaching mass is taken from Eq. (13). Dividing this charge by the mass of the detaching sphere gives us the specific charge of the spray. To find the total spray current, we multiply the specific charge by the massflow of the sprayer, which yields Eq. (14):

$$I_s = Q_r \frac{3\dot{m}}{4\pi\rho_d R_r^3} = \frac{-3}{4\pi}\frac{\psi_e \dot{m}}{\rho_d k R_l^2 a^2 (1+a)}\left[\gamma + F\left(\frac{1}{1+a}\right)\right] \tag{14}$$

Here $\dot{m}$ denotes the spray massflow and ρ_d the droplet density. Fig. 3 shows the normalised spray current as a function of diameter ratio a. For a smaller than unity the figure shows an inverse linear relation between droplet size and total spray current, progressing to an inverse square relation for a larger than unity.

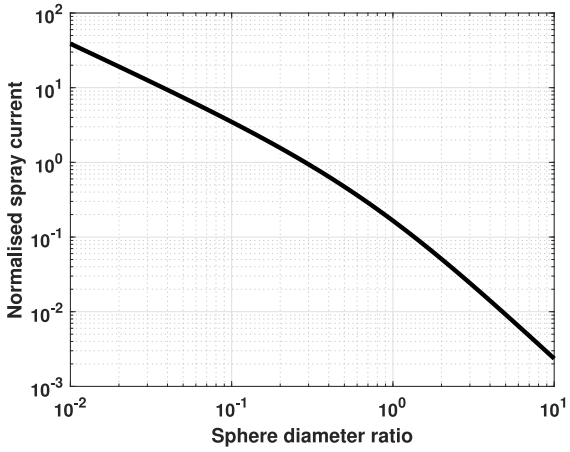

Fig. 3. Normalised spray current, $I_s \rho_d k R_l^2 / \psi_e \dot{m}$, as a function of diameter ratio a.

2.3. Electric potential as a function of spray current

To find an expression for the droplet-induced potential at the injector as a function of spray current, following Eq. (4), we must solve the Poisson equation (2). To do so we need to know the charge density distribution in the domain, which requires knowing the trajectories of the spray droplets. Since we intend to predict droplet charge for numerical simulations, it makes sense to couple this step with the CFD and droplet tracking solver. We discuss an implementation of Lagrangian charged droplet tracking using the Ansys Fluent CFD solver in our previous article [10], which we will again use for the present simulations.

For the droplet charge model we need to compute both the combined electric field Ψ as well as the electric field component due to droplet charge Ψ_d. The combined field is necessary to compute the droplet trajectories, and can be solved exactly as in our previous article [10]. The latter is needed to compute ψ_d as a function of spray current I_s, and to that end we will solve a second "virtual" potential field $\hat{\Psi}_d = \Psi_d / I_s$. To solve this virtual field we need a virtual charge density $\hat{\rho}_q$, which is made up of the virtual charges carried by the droplets present in the domain. Thus, for each droplet we need to set a virtual charge $\hat{q}_d = q_d / I_s$.

2.3.1. Individual droplet charge

The initial charge of individual droplets in a charged spray is not simply proportional to the droplets' volume. According to Viti et al. [3], various scaling laws have been proposed. We follow the example of Viti [3], and others including Domnick et al. [14] and Guettler et al. [4], and use $q_d \propto \sqrt{r_d^3}$. This scaling is proportional to the Rayleigh stability limit for charged droplets. The constant of proportionality can be determined by demanding that the sum of all individual droplet charges produced per second matches the spray current. If the droplet sizes follow the Rosin–Rammler distribution, with a reference radius r_0 and spread parameter n, the initial charge of individual droplets is given by Eq. (15). We use the scaling exponent $b = \frac{3}{2}$, but this equation will hold for any value between 0 and 3.

$$q_d = C_1 r_d^b \quad \text{with} \quad C_1 = \frac{4\pi}{3} \frac{\rho_d I_s}{\dot{m}} \frac{r_0^{(3-b)}}{\Gamma(1 - \frac{(3-b)}{n})} \tag{15}$$

Other droplet size distributions can be used in conjunction with our general method, but will require the user to calculate the corresponding charge distribution.

2.3.2. Virtual droplet-induced potential field

The virtual droplet-induced field is found by solving the Poisson equation, with the same boundary conditions as specified in Table 1 for Ψ_d. The value of $g(...)$ is then found by taking the virtual electric potential at the sprayer nozzle. Some examples of the virtual potential field solution are given in Sections 3.2.2 and 3.3.2.

2.4. Combined model

With the provided methods for finding values for $f(...)$ and $g(...)$, the spray current can be computed according to Eq. (6). We suggest recomputing the spray current, and thus droplet charges, whenever new Lagrangian parcels are injected into the simulation. Each change in charge will result in (slight) changes in droplet trajectories and thus the value of $g(...)$, until the simulation converges on the final solution. We find that, since Eq. (6) is a direct rather than an iterative expression, including it in an existing Euler–Lagrange solver does not contribute to numerical instabilities.

So far unmentioned is the "remaining" potential component, Ψ_0. In cases involving direct-charging sprayers, where only the nozzle is electrified and all other conductors are grounded, this field component is trivially zero everywhere. This is not the case for inductively charged sprayers, in which one or more electrodes are placed near the nozzle. If such electrodes are present, Ψ_0 must also be computed, by again solving the Poisson equation with the boundary conditions as specified in Table 1.

2.4.1. Scaling considerations

The scaling of Eq. (6) for the spray current changes asymptotically depending on the value of the product of $f(...)$ and $g(...)$. For $fg \ll 1$, the equation reduces to $I_s = (\psi - \psi_0) f(...)$, making the space charge distribution irrelevant. Such a situation might occur in inductively-charged spray systems, although Cooke et al. [15] find that space charge can significantly affect those as well, despite the close spacing of the nozzle and induction electrode.

Vice versa, if $fg \gg 1$, the equation reduces to $I_s = (\psi - \psi_0) g(...)^{-1}$. This situation is more likely in large-scale conductively-charged spray systems, and favours the use of our spray charge model. With our approach, the value of $g(...)$ can be calculated to great accuracy, while $f(...)$ can only be estimated or calculated from measurement data.

3. Validation study

To validate our approach and demonstrate its versatility we simulate two sprays for which experimental results are available. We have selected the experimental studies by Marchewicz et al. [11] and Anestos et al. [16] as the most suitable sources for validation data. These studies in particular stand out by including sufficiently detailed descriptions of the spray properties and geometry to be replicated numerically. Furthermore, the sprays in both studies are good representatives of the high-flowrate and directly charged types that our model is intended for. Finally, for the sake of demonstrating versatility, both sprays differ greatly from each other in terms of droplet size, flowrate, and electrode geometry.

3.1. Numerical method

For our simulations, we use the Ansys Fluent CFD and DPM solver (version 18). The flow fields are solved using steady RANS equations, and droplet trajectories are computed using quasi-steady Lagrangian tracking. The (virtual) electric potential is solved using the Poisson equation, and is computationally treated as a Eulerian phase. For a comprehensive description of the equations and methods used we refer to our previous work [10], which covers the general simulation framework in detail.

To compute a quasi-steady Euler–Lagrange solution, this solver alternates between two modes. In the Eulerian mode, it iteratively solves the equations governing the Eulerian phases (including the potential fields). In the quasi-steady Lagrangian mode, it uses forward integration to compute the trajectories of Lagrangian parcels. These trajectories are computed all the way from the parcels' injection to the point where they leave the domain. The Lagrangian solver computes the amount of mass, momentum, and energy exchanged between the parcel and the flow, as well as the charge density the parcel represents. It converts these values into volumetric source terms that are then handed back to the Eulerian solver. By alternating (several) Eulerian solver iterations with Lagrangian droplet tracking computation, a converged coupled solution is achieved.

Implementation of our droplet charge prediction model requires a few modifications to the modelling framework presented previously. Two additional electric potential fields are added, representing the virtual potential field $\hat{\Psi}_d$ and the field component Ψ_0. The Lagrangian parcels are modified, adding a variable that represents the virtual charge $\hat{q}_d$ carried by the droplets. Finally, a subroutine is added that computes the spray current and the electric charge carried by the droplets, using Eqs. (6) and (15). This subroutine is called prior to each round of Lagrangian droplet tracking computations. To resolve Eq. (6), the values of ψ_0 and $g(...)$ are computed from the Eulerian field solution, while the values of ψ and $f(...)$ are supplied as user input at the start of the simulation.

3.2. Inductively charged sprayer from Marchewicz et al. [11]

In their work, Marchewicz et al. [11] investigate the spray current for an inductively charged sprayer, pictured in Fig. 4a. They use a pressure atomiser with interchangeable nozzles, placed inside an induction electrode. The setup is enclosed in a cylindrical tube covered in conductive mesh, inside which a cylindrical "Faraday cage" is suspended to serve as a spray target. This cage is connected to ground via an ammeter, which is used to measure the effective spray current.

Fig. 4b shows our numerical domain. To reduce the computational effort required we make use of the symmetry of the setup, and simulate only a quarter of the full cylindrical geometry. Marchewicz et al. [11] describe their sprayer and setup geometry comprehensively, allowing us to replicate the main features accurately.

Table 2
Spray parameters, Case 1.

Nozzle type	Lechler 460.523
Spray geometry	45° full cone
Flowrate	3.21 [L/min]
Droplet reference radius	$r_0 = 185$ [μm]
Spread parameter	3.5
Initial velocity	32 [m/s]
Electrode geometry	Toroidal, 100 × 12 [mm]
Electrode offset	[0, 20, 40] [mm]
Electrode voltage	−10 [kV]
Spray current function	$f(...) = 1.27 \times 10^{-8}$ [A/V]

3.2.1. Case description

Marchewicz et al. [11] performed a vast series of measurements, primarily varying the voltage, position, and geometry of the electrode, as well as using different models of nozzle. Since the measured specific charge shows very similar scaling with electrode voltage for each configuration, we will only show detailed simulation results for a single case. Furthermore, since our model by definition gives a linear relation between spray current and electrode voltage we choose to simulate at 10 kV, which is high in the linear range for Marchewicz's data. We use a Rosin–Rammler droplet size distribution, which reasonably approximates the measured droplet sizes. The full set of case parameters we use is given in Table 2.

To estimate the value of the spray current function $f(...)$ we use Eq. (14). We use the nozzle bore radius (0.75 mm) and droplet reference radius ($r_0 = 185$ μm) as our "bulk" and "breakoff" representative radii. This yields a value of $f(...) = 1.27 \times 10^{-8}$ Ampere per Volt.

3.2.2. Solution

Since this case involves an electrified induction electrode the Ψ_0 field component will not be trivial, and need to be solved to find ψ_0. This potential field, as well as the virtual droplet induced potential $\hat{\Psi}_d$ and the total potential Ψ are shown in Figs. 5a, 5b and 5c. These fields, for the case with a 20 mm electrode offset, are plotted on a (half) cross-section of the domain, in the plane intersecting the induction-electrode support. For the sake of brevity, we omit showing the gas phase results in this article, which are wholly unremarkable for a spray-entrained airflow.

The plotted figures illustrate the boundary- and field-conditions applied to the different potential components. The Ψ_0 component is

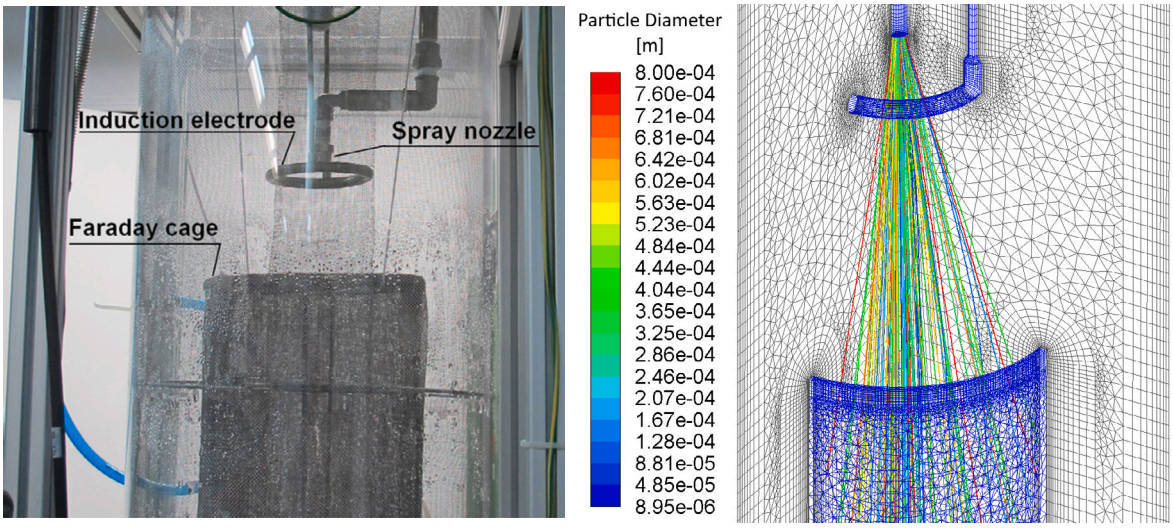

(a) Experimental setup, from Marchewicz et.al.[11]

(b) Numerical domain and simulated droplet trajectories

Fig. 4. First validation case, experimental setup and numerical model.

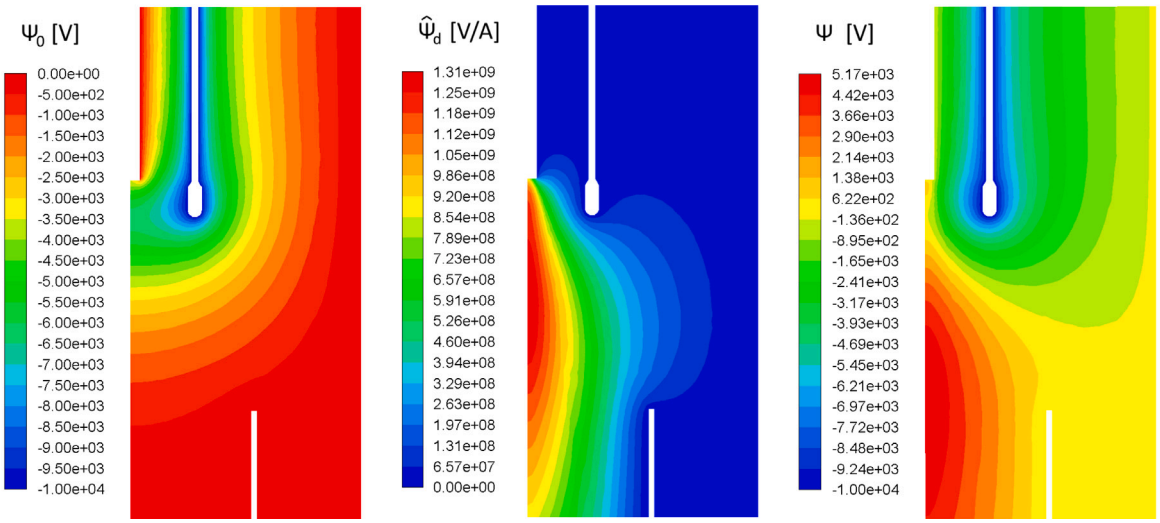

(a) Electrode potential component Ψ_0 (b) Spray-induced virtual potential $\hat{\Psi}_d$ (c) Combined potential field Ψ

Fig. 5. Computed potential (component) fields for the first validation case, with 20 mm electrode offset.

zero at all (conductive) boundaries, except the induction electrode and the injector face. The $\hat{\Psi}_d$ component is zero at the induction electrode as well, but shows a high value in the centre of the spray cone, away from all boundaries. The effects of both components are evident in the combined field Ψ. Although not immediately apparent from the figure, the net electrostatic flux over the injector face is slightly positive, courtesy of the (not plotted) Ψ_e component that also generates the droplet charges. The potential fields for electrode offsets of 0 and 40 mm are qualitatively similar, albeit with slightly different values at the injector face.

3.2.3. Results

The electrode induced potentials and spray-induced virtual potentials at the injector face for different electrode offsets are shown in Fig. 6a. These potentials are used to compute the spray current, which is plotted in Fig. 6b, compared to the values measured by Marchewicz et al. [11]. In this figure we also plot the "spacecharge-limited" spray current, which is the value that is obtained under the assumption that $fg \gg 1$ (see Section 2.4.1).

From Fig. 6a we can see that both the electrode-induced potential and the droplet induced potential at the nozzle varies with the electrode offset. ψ_0 likely has a maximum at an offset between 0 and 20 mm, when the electrode is closest to the injector face without being occluded by the grounded supply tube. ψ_d decreases with increasing electrode offset, as the electrode is "pushed into" the space-charge cloud.

Fig. 6b shows that our model gives a reasonable first-order prediction of the spray current in this case. Even if we disregard our approximate value for $f(...)$, the spacecharge-limited prediction is perhaps even closer to the measured values. However, this figure also makes clear that the model does not predict the measured variation of spray current with the electrode offset. We expect that this difference can be attributed to two mechanisms. The first is that the bulk of water coming from the nozzle effectively acts as an extension of the nozzle geometry. The jet forms a sharper point than the nominally blunt nozzle, which will increase the electric field strength near the primary breakup point, and its variation with the electrode offset distance. This effect might be included in a simulation, by changing the nozzle geometry to match photographs of the water at the nozzle exit. The second effect is corona discharge; a smaller distance between nozzle and electrode results in increased negative discharge from the electrode, partly neutralising the spray and reducing the measured spray current. Marchewicz [11] mentions this effect, and is corroborated by Higashiyama [17] and Castle and Inculet [18], but our present model cannot estimate it quantitatively.

Table 3
Spray parameters, Case 2.

Nozzle type	Ransburg 4907-2, #5 air cap
Spray geometry	60° × 15° Elliptical full cone
Flowrate	[108, 185, 250] [g/min]
Droplet reference radius	$r_0 = 21.5$ [μm]
Spread parameter	3.5
Initial droplet velocity	[25–32] [m/s]
Nozzle air velocity	[25–32] [m/s]
Nozzle voltage	60 [kV]
Spray current function	$f(...) = 4.6319 \times 10^{-9}$ [A/V]
	$f(...) = 7.9343 \times 10^{-9}$ [A/V]
	$f(...) = 1.0722 \times 10^{-8}$ [A/V]

3.3. Directly charged sprayer from Anestos et al. [16]

Anestos et al. [16] investigate a directly charged spray created using an air-assisted atomiser. Intended to represent charged paint application, a square target plate with a side of 406 mm (16″) was placed 305 mm (12″) in front of the sprayer nozzle. No photographs of the setup are provided, so our numerical representation shown in Fig. 7 is based on the description only. To model the effects of the air blast from the atomiser, air is injected from the atomiser face along with the spray droplets. As with the first validation case, we will simulate only a quarter of the full geometry to reduce computational effort.

3.3.1. Case description

Anestos et al. [16] vary a number of parameters throughout their measurements, the most relevant and influential of which is the liquid flowrate. Unfortunately, they only provide the measured total spray current at a constant liquid flowrate of 185 g/min. For the remaining values of liquid flowrate, we will compare our results to the specific charge measured by Anestos et al. [16]. The spray parameters for the simulated cases are given in Table 3.

We estimate the value of the spray current function $f(...)$ using Eq. (14). The nozzle bore radius (0.762 mm, 0.06″) and the droplet reference radius (21.5 μm) are again used as the representative radii. This yields values of $f(...) = 4.6319 \times 10^{-9}$, 7.9343×10^{-9}, and 1.0722×10^{-8} Ampere per Volt at 108, 185, and 250 g/min liquid flowrate respectively.

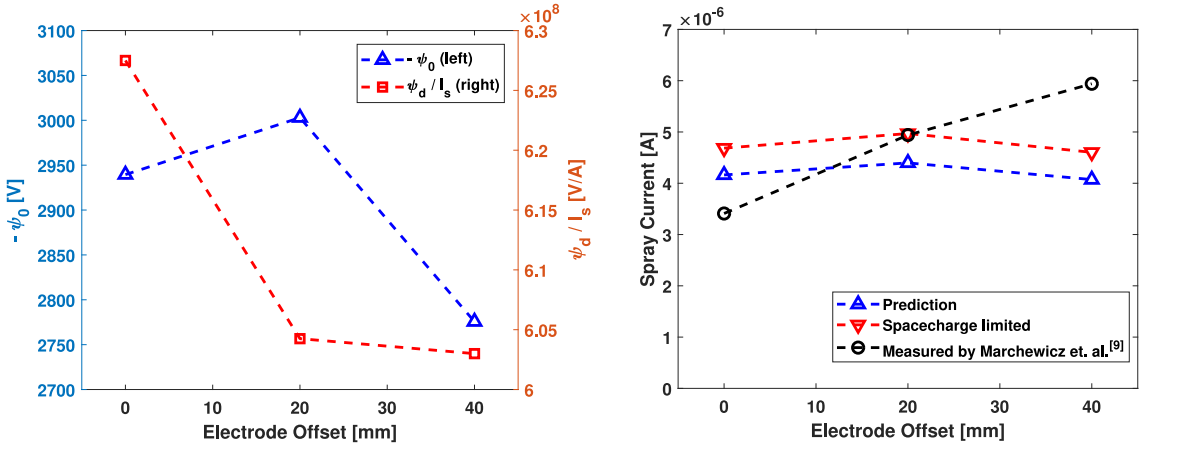

(a) Simulated potential components at the injector face (b) Spray current, simulation compared to Marchewicz et. al.[11]

Fig. 6. Results from the first validation case.

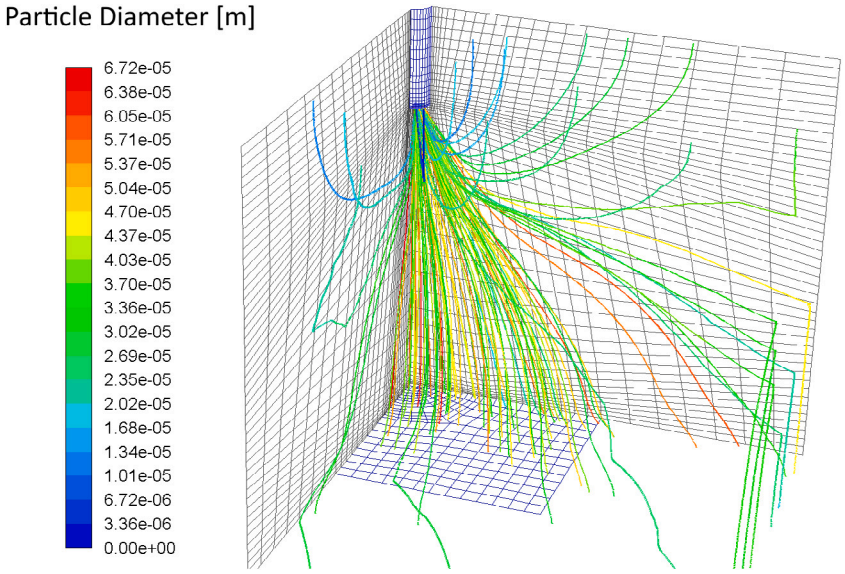

Fig. 7. Second validation case, numerical domain and particle tracks coloured by droplet diameter, at 185 g/min liquid mass flow.

3.3.2. Solution

Since this case does not involve any electrodes besides the sprayer nozzle itself, the Ψ_0 field component is trivially zero throughout the domain. The droplet charge is thus determined solely by the value of $f(...)$ and the virtual droplet-induced potential. This virtual potential field $\hat{\Psi}_d$ is shown in Fig. 8, plotted on both symmetry planes of the geometry, for the case with 185 g/min liquid flowrate. The combined electric potential Ψ for the same flowrate is also plotted, in Fig. 9. These (virtual) potential fields are shaped as expected, high near the sprayer nozzle and dropping outward towards the grounded box enclosing the experiment. The high potential region is wider in the X direction than in the Z direction, caused by the flattened-cone shape of the spray being oriented along the XY plane. For different values of liquid flowrate the shape of the (virtual) electric field does not change appreciably, and the maximum value of $\hat{\Psi}_d$ increases slightly for increasing flowrate and vice versa.

Although the gas-phase solution is as unremarkable in this case as in the previous one, it would go amiss not to comment on the particle tracks shown in Fig. 7. A large fraction of the droplets, especially those with relatively small diameters, exit the domain without hitting the target. The reason for this can be seen in Fig. 9, which shows a high electric potential in the middle of the domain, repelling droplets in all directions. Integrating the droplet deposition rate over the target plate we find a total liquid transfer rate of 116 gram per minute out of 185 g/min supplied to the sprayer. This matches Anestos' [16] observations, who estimates a liquid transfer rate of 110 g/min in their experiments.

3.3.3. Results

Anestos et al. [16] present total spray current as a function of the conductivity of the liquid. At low conductivities, the spray current (and therefore droplet charge) is reduced due to the electric relaxation becoming too slow to fully charge droplets before they detach from the liquid bulk. At high conductivities the droplet charge is reduced as well, while the total injector current remains constant due to increased corona discharge from the liquid surface. Since our model does not incorporate conductivity or corona discharge, we will compare our spray current to the maximum current measured by Anestos. This maximum is 18 μA, and is only given for a liquid flowrate of 185 g/min.

From our simulation results at 185 g/min liquid flowrate we find that the droplet-induced virtual potential at the injector is 3.11 Gigavolt per Ampere. Substituting this and the value of $f(...)$ into Eq. (6), our model predicts a spray current of 18.54 μA. For reference, we can also compute the "spacecharge-limited" value by dividing the nozzle voltage by $\hat{\psi}_d$, resulting in a value of 19.29 μA. Both these predictions

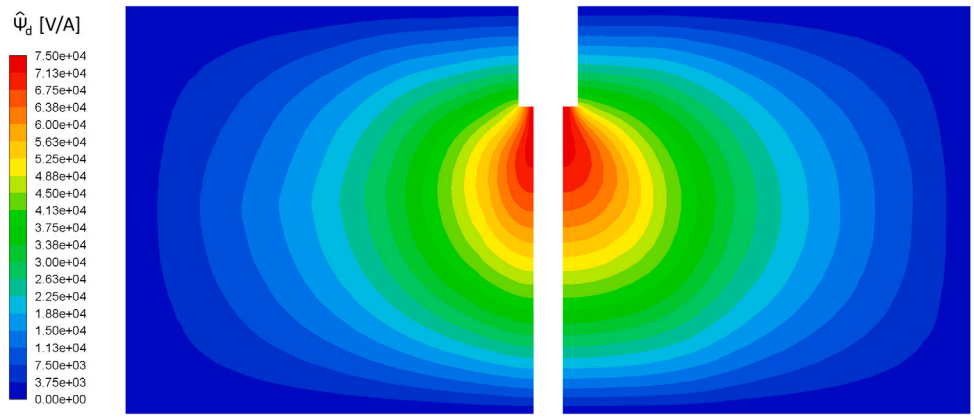

Fig. 8. Second validation case, virtual droplet induced potential $\hat{\Psi}_d$ on the ZY-plane (left) and XY-plane (right), at 185 g/min liquid flowrate.

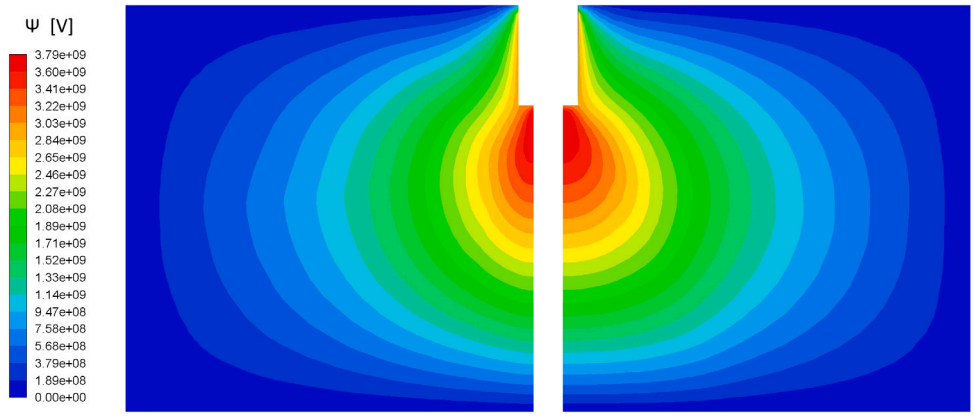

Fig. 9. Second validation case, electric potential Ψ on the ZY-plane (left) and XY-plane (right), at 185 g/min liquid flowrate.

are extremely close to the value measured by Anestos et al. [16], with only a slight overprediction. An overprediction was to be expected in this case, since Anestos does measure a notable amount of corona-discharge current. Corona discharge increases the amount of space-charge present, further suppressing the effective nozzle potential and thereby reducing the spray current.

To compare our results at different liquid flowrates, we extract the massflow-averaged specific charge from the figures presented by Anestos et al. [16]. The comparison between these experimental values and our prediction of average specific charge at the target plate is shown in Fig. 10. As can be seen in the figure, our prediction follows the trend of increasing specific charge at lower liquid flowrates, and stays within one standard deviation from Anestos' data. We do see that Anestos finds a particularly high variation in specific charge for the case with 108 g/min liquid flow, but a more detailed characterisation of the used sprayer would be required to explain this behaviour.

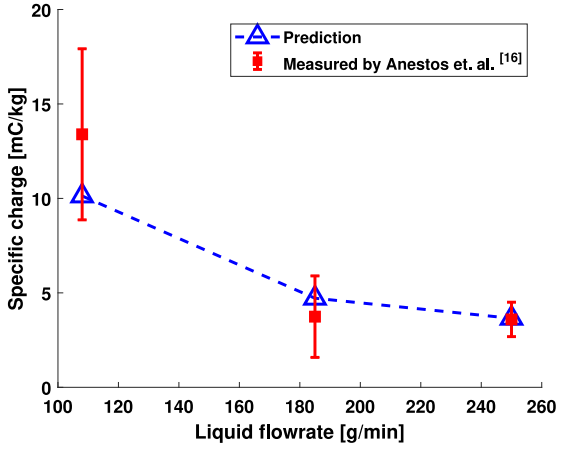

Fig. 10. Second validation case, average specific charge at the target as a function of liquid flowrate, compared to data from Anestos et al. [16].

4. Conclusions

In this work we developed a novel method for estimating droplet charges in directly charged sprays. This method is primarily based on separation of the electric field into distinct components that can be attributed to the spray nozzle, to the space charge effect of the charged droplets, and to all remaining electrodes respectively. The droplet charge is found by balancing these field components such that all electrostatic boundary conditions are satisfied. This approach requires no prior knowledge of the electrical properties of the spray(er) in question, and can be applied to most arbitrary systems and geometries.

The presented method does not require resolving the spray-breakup process in detail, and only adds two global field variables for which the Poisson equation must be solved. This allows it to be implemented into any simulation of high-flowrate charged sprays, such as those used for spray painting, gas scrubbing and other industrial applications. The implicit formulation of the expression for the spray current prevents the introduction of numerical instabilities.

Our validation study shows that the presented method can predict the droplet charge within reasonable accuracy. This is true for both tested validation cases, despite differences in spray parameters of up to an order of magnitude. Our method can therefore be a powerful and

versatile tool for estimating the performance of electrostatic sprayers in new applications, and for improving the accuracy of simulations of electrostatic sprays in moving or changing geometries.

Declaration of competing interest

The authors declare that they have no known competing financial interests or personal relationships that could have appeared to influence the work reported in this paper.

Acknowledgement

This work is supported by the EFRO Oost-Nederland programme, The Netherlands within the CrestCool project (# PROJ-00730).

References

[1] A. Jaworek, A. Krupa, Charged Sprays Generation and Application, in: Sprays: Types, Technology and Modeling, Nova Science Publishers Inc., 2011, pp. 1–100.
[2] K.R. Ellwood, J. Braslaw, A finite-element model for an electrostatic bell sprayer, J. Electrost. 45 (1) (1998) 1–23.
[3] V. Viti, J. Kulkarni, A. Watve, Computational fluid dynamics analysis of the electrostatic spray painting process with a rotating bell cup, At. Sprays 20 (1) (2010) 1–17.
[4] N. Guettler, P. Knee, Q. Ye, O. Tiedje, Initial droplet conditions in numerical spray painting by electrostatic rotary bell sprayers: A framework for optimization of injection model coefficients, J. Coat. Technol. Res. (1) (2020).
[5] A. Mark, B. Andersson, S. Tafuri, K. Engstrom, H. Sorod, F. Edelvik, J.S. Carlson, Simulation of electrostatic rotary bell spray painting in automotive paint shops, At. Sprays 23 (1) (2013) 25–45.
[6] J. Domnick, A. Scheibe, Q. Ye, The simulation of electrostatic spray painting process with high-speed rotary bell atomizers. Part II: External charging, Part. Part. Syst. Charact. 23 (5) (2007) 408–416.
[7] R.T. Collins, J.J. Jones, M.T. Harris, O.A. Basaran, Electrohydrodynamic tip streaming and emission of charged drops from liquidcones, Nat. Phys. 4 (2) (2008) 149–154.
[8] M.A. Herrada, J.M. López-Herrera, A.M. Gañán-Calvo, E.J. Vega, J.M. Montanero, S. Popinet, Numerical simulation of electrospray in the cone-jet mode, Phys. Rev. E 86 (2) (2012) 1–8.
[9] W. Wei, Z. Gu, S. Wang, Y. Zhang, K. Lei, K. Kase, Numerical simulation of the cone-jet formation and current generation in electrostatic spray - Modeling as regards space charged droplet effect, J. Micromech. Microeng. 23 (1) (2013).
[10] A. Brentjes, A.K. Pozarlik, G. Brem, Numerical simulation of evaporating charged sprays in spray chilling, J. Electrost. 107 (September) (2020).
[11] A. Marchewicz, A.T. Sobczyk, A. Krupa, A. Jaworek, Induction charging of water spray produced by pressure atomizer, Int. J. Heat Mass Transfer 135 (2019) 631–648.
[12] A. Tikhonov, A. Samarski, Equations of Mathematical Physics, in: Dover Books on Physics, Dover Publications, 1990.
[13] M. Abrahamowitz, I.A. Stegun, Handbook of Mathematical Functions, tenth print, Dover Publications, New York, 1972.
[14] J. Domnick, A. Scheibe, Q. Ye, The simulation of the electrostatic spray painting process with high-speed rotary bell atomizers. Part I: Direct charging, Part. Part. Syst. Charact. 22 (2) (2005) 141–150.
[15] J.R. Cooke, S.E. Law, Finite-element analysis of space-charge suppression of electrostatic-induction spray charging, 37 (3) (2001) 751–758.
[16] T.C. Anestos, J.E. Sickles, R.M. Tepper, Charge to mass distributions in electrostatic sprays, IEEE Trans. Ind. Appl. IA-13 (April) (1977) 168–177.
[17] Y. Higashiyama, S. Tanaka, T. Sugimoto, K. Asano, Size distribution of the charged droplets in an axisymmetric shower, J. Electrost. 47 (3) (1999) 183–195.
[18] G. Castle, I. Inculet, Induction charge limits of small water droplets, in: The 8 th International Conference on Electrostatics 1991, Oxford, Engl, 04/10-12/91, 1991, pp. 141–146.